Materials & Design 265 (2026) 115993

Contents lists available at ScienceDirect

Materials & Design

journal homepage: www.elsevier.com/locate/matdes

Material extrusion of low-thermal-expansion cordierite ceramics: Process optimization and performance evaluation by data-driven technique

Pengxian Hui [a,b], Haohao Ji [a,*], Ye Ge [a], Jin Zhao [a], Wenlong Liu [a], Shiwei Wang [a,b], Dianzi Liu [c,d,*], Jian Zhang [a,b,*]

[a] State Key Laboratory of High Performance Ceramics, Shanghai Institute of Ceramics, Chinese Academy of Sciences, Shanghai 200050, China
[b] Center of Materials Science and Optoelectronics Engineering, University of Chinese Academy of Sciences, Beijing 100049, China
[c] College of Engineering, Ocean University of China, Qingdao 266100, China
[d] School of Engineering, University of East Anglia, Norwich NR4 7TJ, UK

ARTICLE INFO

Keywords:
Cordierite ceramic
Material extrusion
Low thermal expansion
Artificial neural network
Latin hypercube sampling

ABSTRACT

Material extrusion of cordierite ceramics faces challenges in fabricating dense, high-strength components due to non-linear parameter coupling. To address this, a two-stage framework based on Latin hypercube sampling is proposed. The first stage employs planar dimensional deviation of green bodies for rapid, non-destructive screening to filter impractical parameters prior to sintering. The second stage optimizes flexural strength of sintered bodies under dimensional constraints, enabling a decoupled enhancement of mechanical performance. Sensitivity analysis reveals that layer height (41.8%) and nozzle temperature (39.0%) govern dimensional deviation, whereas layer height is the dominant factor (60.7%) governing flexural strength, which is further validated by the evolution of microstructural defects. Under optimized conditions, the green bodies achieve a planar dimensional deviation of $<0.25\%$, while the sintered samples reach a flexural strength of 196.8 MPa after hot isostatic pressing. To validate the proposed framework, a 148-mm lightweight mirror is successfully fabricated, exhibiting near-zero thermal expansion (-0.45 to 0.05×10^{-6}/K, 0–50 °C). This study provides a useful insight into the development of a data-driven fused deposition modeling strategy for the fabrication of high-performance ceramic components.

1. Introduction

Cordierite ceramic ($Mg_2Al_4Si_5O_{18}$) is a magnesium aluminosilicate ceramic with ultra-low thermal expansion coefficient ($1.5–2.0 \times 10^{-6}$/K, 20–1000 °C), low dielectric loss, and high Young's modulus, exhibiting excellent thermal stability and mechanical properties [1–3]. Compared with common ultra-low expansion glasses, cordierite not only has higher specific stiffness and better thermal stability, but also possesses stronger processing adaptability, making it suitable for the fabrication of lightweight, complex-structured high-precision components. With these advantages, cordierite ceramics demonstrate broad application prospects in high-end fields such as space optics, ultra-precision measurement instruments, integrated-circuit substrates, etc. [4–6].

With the increasing demand for high-density and lightweight cordierite ceramic components in these applications, conventional forming techniques such as dry pressing, slip casting, isostatic pressing, and gel casting [7,8] are gradually receiving less attention due to potential limitations. These conventional methods are highly mold-dependent, limit design flexibility, exhibit low material utilization, and thus fail to meet the requirements for efficient fabrication of complex ceramic structures [9]. In contrast, ceramic additive manufacturing (AM) technologies, including material extrusion (MEX), vat photopolymerization (VPP), binder jetting (BJT), and powder bed fusion (PBF), are well developed for rapid forming of complex structures [10–14]. Among these approaches, fused deposition modeling (FDM), a representative MEX technique, is an indirect ceramic additive manufacturing technology that prepares feedstock by mixing ceramic powder with the polymer binder, then extrudes and deposits it layer by layer through a nozzle after heating and melting, and finally produces

---

[*] Corresponding authors at: State Key Laboratory of High Performance Ceramics, Shanghai Institute of Ceramics, Chinese Academy of Sciences, Shanghai 200050, China (H. Ji); College of Engineering, Ocean University of China, Qingdao 266100, China (D. Liu); State Key Laboratory of High Performance Ceramics, Shanghai Institute of Ceramics, Chinese Academy of Sciences, Shanghai 200050, China (J. Zhang).

E-mail addresses: jihaohao@mail.sic.ac.cn (H. Ji), Dianzi.Liu@uea.ac.uk (D. Liu), jianzhang@mail.sic.ac.cn (J. Zhang).

https://doi.org/10.1016/j.matdes.2026.115993
Received 27 December 2025; Received in revised form 1 April 2026; Accepted 10 April 2026
Available online 13 April 2026

the ceramic component through debinding and sintering [15]. This technique offers distinct advantages, including low cost, operational stability, and recyclability of feed materials. In recent years, Li et al. [16] have fabricated a 200 mm-diameter silicon carbide mirror using FDM combined with reaction sintering, while Shen et al. [17] have achieved zirconia components with a relative density of up to 99%, thereby demonstrating the considerable potential of FDM in applications for structural ceramics.

However, the forming quality of components produced by FDM is strongly influenced by the nonlinear coupling of process parameters, such as the printing speed, nozzle temperature, filling density, and layer thickness [18]. It is noted that achieving stable, high-quality fabrication of complex structures typically requires a vast number of parameter combinations and tedious trial-and-error adjustments [19,20]. Moreover, ceramic FDM must be accompanied by critical post-processing steps, including debinding and sintering, which result in more processing cycles and substantial material consumption, thereby significantly increasing the experimental cost and time burden [21]. Therefore, traditional single-factor approaches are inadequate for capturing multi-parameter interactions and guiding systematic optimization.

To address the aforementioned challenges, it is imperative to develop an experimental methodology with high-efficiency modeling capabilities and intelligent computation features. The artificial neural network (ANN), owing to its self-adaptive learning and deep mapping capabilities, has demonstrated significant advantages in the modeling and optimization of multi-parameter coupled systems [22,23]. In ceramic research, ANN has proven effective across critical processing stages. Deng et al. [24] utilized ANN to optimize alumina slurry formulation and extrusion behavior for ceramic 3D printing. Andrade et al. [25] developed an ANN-based infrared thermal imaging system for the defect detection in sintered products, while Scott et al. [26] validated the feasibility of ANN in determining the composition-property dependencies of dielectric ceramics. Compared with response surface methodology and support vector regression, ANN is not constrained by fixed polynomial assumptions and offers greater architectural flexibility for modeling complex interactions [27,28]. However, the efficacy of such data-driven models is fundamentally determined by the quality of the dataset. Given the high time–cost of ceramic post-processing, traditional full factorial design is experimentally prohibitive due to the exponential growth of sample size [29]. While orthogonal arrays are efficient for linear problems, they often lack the global data density required for non-linear modeling [28]. Furthermore, simple random sampling entails the risk of stochastic aggregation, failing to adequately represent the global domain [30]. To resolve this, Latin hypercube sampling (LHS) is employed in this study. By stratifying the input parameter ranges, LHS offers superior space-filling and non-collapsing capabilities, which ensures uniform distribution without redundancy. This maximizes the information extracted from a limited number of experiments, making it an ideal strategy for training ANN models to resolve non-linear coupling effects [31]. Despite these advantages, studies on ANN-based optimization of ceramic FDM remain relatively limited, especially with respect to systematic approaches that integrate LHS-based experimental screening with predictive modeling for process exploration and performance evaluation.

Based on the LHS-designed experimental dataset, a two-stage methodological framework is proposed to achieve efficient process exploration and performance evaluation of the cordierite ceramic FDM process. In the first stage, planar dimensional deviation is developed as a rapid and non-destructive indicator for assessing printing quality. Then, to improve experimental efficiency given the long sintering cycle and high cost of ceramic testing, a PDD-ANN (planar dimensional deviation-based ANN) model is constructed based on green bodies data. This model is used to identify the dominant process parameters within the feasible parameter space while maintaining the deposition stability and surface integrity. This stage serves to efficiently eliminate impractical parameter combinations, thereby reducing both the experimental workload and the time for subsequent mechanical tests. In the second stage, three-point flexural strength is adopted as the performance metric. Following that, a FS-ANN (flexural strength-based ANN) model is developed to capture the relationship between process variables and structural properties. This enables the overall preparation of cordierite ceramics with improved densification and mechanical performance. Finally, through the integration of hot isostatic pressing (HIP), dense and high-strength cordierite ceramic components are successfully fabricated, indicating the reliability of the proposed strategy and underscoring its potential for broader applications in ceramic additive manufacturing.

2. Experimental methodology

2.1. Feedstock preparation

The feedstock was composed of cordierite powder and a multi-component binder system. The cordierite powder had an average particle size of 2.2 μm and a BET surface area of 7.6 m^2/g. The binder system included three parts: 1) Low molecular weight binder – Paraffin wax (PW, Sinopharm Chemical Reagent Co., China) functioned as the primary diluent to reduce viscosity and ensured sufficient flowability for printing geometrically complex parts with high dimensional accuracy; 2) High molecular weight binders – Polyethylene (PE, Formosa Plastics Co., China) and ethylene–vinyl acetate (EVA, DuPont, USA) acted as backbone polymers to provide structural integrity to the green parts during debinding; 3) Additives – Stearic acid (SA, PT. SUMI ASIH, Indonesia) served as a surfactant to improve powder–binder compatibility, and dioctyl phthalate (DOP, Sinopharm Chemical Reagent Co., China) was used as a plasticizer to enhance binder flexibility and ductility. The solid loading of cordierite was 75 wt% and the mass ratio of binder components was set to 30:9:48:2:1 for the sequence PE: EVA: PW: SA: DOP. Prior to mixing, the cordierite powder was dried in a vacuum oven at 80 °C for 24 h to completely remove adsorbed moisture. All components were weighed accordingly. The solid binders were first added to an internal mixer (Sublimation 3D, China) preheated to 170 °C. After melting, the ceramic powder was introduced and mixed thoroughly with the molten binder, followed by sequential addition of SA and DOP. Mixing continued at a rotor speed of 40 rpm for 60 min to ensure homogeneity. The compound was then cooled and crushed by a jaw crusher (Sublimation 3D, China). To ensure stable feeding and uniform melting during the extrusion process, the feedstock was sieved to a range of 4–8 mesh.

2.2. Material extrusion printing

3D models of the specimens were designed and sliced using UPRISE 3D software (Sublimation 3D, China), in which process parameters such as the layer height, nozzle temperature, printing speed, and extrusion flow rate were specified to generate the corresponding G-code. The G-code was then uploaded to an UP-556 FDM printer (Sublimation 3D, China) for fabrication. During printing, the nozzle diameter was 1.0 mm, the build plate temperature was maintained at 100 °C, and blue painter's tape was applied to the surface to enhance first-layer adhesion. The infill density was set to 100%. To ensure uniform structural strength, the printing path was configured with a rectilinear infill pattern (0°/90° raster angle). The prepared feedstock was loaded into the printer, and material deposition was then carried out by layer-by-layer printing with the predefined parameter combinations, as illustrated in Fig. 1.

2.3. Design of process parameterization

This study first conducted a printability validation experiment on the feedstock to ensure that it had sufficient flowability and deposition stability, allowing continuous extrusion and reliable printing of basic

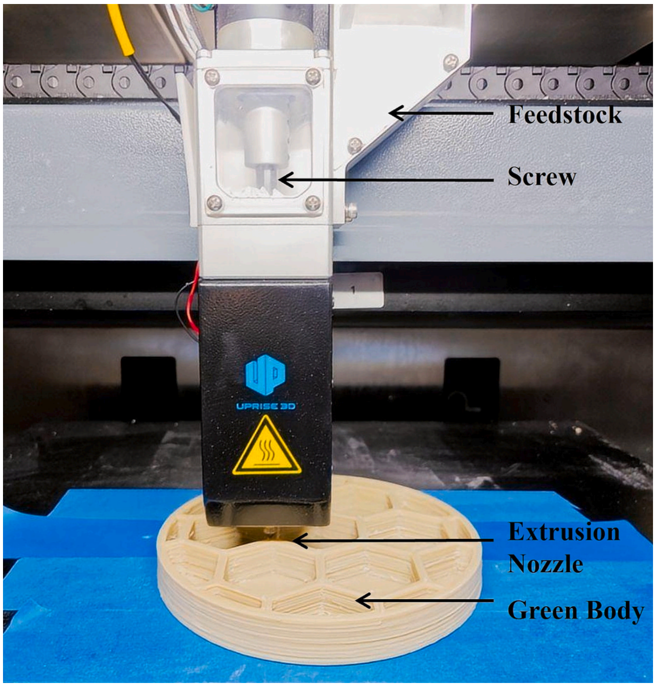

Fig. 1. Photograph of cordierite mirror printing process.

test parts. Following that, a single-factor design of experiments was carried out with four parameters: the layer height (H), extrusion flow rate (Q), printing speed (V), and nozzle temperature (T). Specifically, H denotes the nozzle step distance in the Z-direction (mm), Q represents the ratio of the actual extruded volume to the theoretical path volume (%), V corresponds to the nozzle movement speed in the XY-plane (mm/s), and T refers to the heating temperature at the nozzle (°C). Based on the single-factor analysis, the feasible range of each parameter was determined. A LHS scheme was subsequently employed to generate 40 parameter combinations across four factors and five levels. Under each condition, green bodies were fabricated using the UP-556 FDM printer. The planar dimensional deviation (δ) is defined as follows:

$$\delta = \frac{|L_m L_d|}{L_d} \times 100\% \tag{1}$$

where L_m represents the average measured dimension in the XY-plane, obtained from three measurements on each specimen. L_d denotes the reference dimension considering material shrinkage, which is determined by adjusting the original design value based on the physical shrinkage rate characterized along the Z-axis.

The planar dimensional deviation served as the output variable for constructing the PDD-ANN model. This model was designed to rapidly identify the dominant parameters governing the external quality of printed green bodies and to define a constrained process window for subsequent sintering-stage studies. By focusing on the green body stage, this approach enabled efficient early-stage parameter screening with lower cost and shorter experimental cycles.

Subsequently, based on the results of the above planar dimensional deviation analysis using the PDD-ANN model, Q was excluded due to its limited influence on dimensional accuracy. A three-factor, five-level LHS design was then employed to generate 30 parameter sets for cost-effective experiments. The samples were printed, debinded, and sintered, followed by three-point bending tests to determine the flexural strength (σf). These data were used to further develop the FS-ANN model, which was able to capture the nonlinear relationship between process parameters and the mechanical properties of the sintered ceramics. The optimal parameter combination determined using this model enabled the fabrication of highly dense cordierite ceramics with enhanced flexural performance.

2.4. Debinding and sintering

Using the optimal parameter combination in Section 2.3, the printed green bodies were subjected to solvent debinding by immersion in n-heptane (Macklin, China) at 50 °C for 36 h with a solid-to-liquid volume ratio of 1:10. Then, the specimens were dried in a constant-temperature oven at 50 °C for 24 h. Subsequently, thermal debinding was performed in a muffle furnace (CWF 12/13, Carbolite Ltd, UK). During thermal debinding, the temperature was raised from room temperature to 180 °C at a rate of 3 °C/min, then further from 180 °C to 600 °C at 1 °C/min, and finally the specimens were held at 600 °C for 3 h. Following that, sintering was carried out to heat at 2.5 °C/min to 1420 °C in a muffle furnace (MF1700C, Beiyike Corporation, China), where the samples were held for 2 h and cooled naturally in the furnace. After sintering, some samples were hot isostatic pressed (HIPed) at 1310 °C for 2 h with argon gas pressure of 130 MPa.

2.5. Characterization process

A digital vernier caliper (0.01 mm accuracy) was used to measure Lm and Ld. For Lm, it was averaged from three XY-plane measurements, while Ld was the average of measurements in the Z-direction. Microstructural characterization was performed using a digital microscope (VHX7100, Keyence, Japan) and a field emission scanning electron microscope (Verios G4, FEI Corporation, USA). Thermogravimetric and differential scanning calorimetry (TG-DSC) analyses were conducted using a thermal analyzer coupled with a mass spectrometer (STA449C, Netzsch Inc., Germany) at a heating rate of 10 °C/min up to 800 °C in air. The density of the sintered specimens was determined by Archimedes' method. Rheological properties of the feedstock were measured by a capillary rheometer (Rosand RH2000, Malvern, UK). According to the GB/T 6569–2006 standard for the flexural strength testing of fine ceramics, three-point bending tests were carried out on a universal testing machine (INSTRON-1195, Instron Co., USA). Test specimens with the dimensions of 3 mm × 4 mm × 36 mm were subject to a loading displacement rate of 0.5 mm/min and a span of 30 mm. The reported flexural strength was determined by the average value of five measurements. The statistical reliability of the flexural strength was evaluated using Weibull analysis. The Weibull modulus and characteristic strength were obtained by fitting the measured strength data to the two-parameter Weibull distribution.

3. Results and discussion

3.1. The printability of feedstock

To avoid defects such as filament breakage, nozzle clogging, or layer inconsistencies in the printing process, the printability of the feedstock was evaluated through rheological characterization to verify the stability and flow adaptability of the extrusion process. The relationships between the shear viscosity and shear rate of the feedstock at 155 °C, 165 °C, 175 °C, 185 °C, and 195 °C are shown in Fig. 2. Based on the observations, the feedstock at all temperatures exhibits typical shear-thinning behavior characteristic of power-law fluids: as the molten feedstock passes through the printing nozzle, the increased shear rate leads to a decrease in viscosity. This observed shear-thinning behavior is primarily attributed to the disentanglement and preferential orientation of polymer binder chains along the flow direction under increasing shear rates. Such structural alignment reduces flow resistance and facilitates stable extrusion through the nozzle, which is essential for maintaining continuous material flow during printing while avoiding excessive extrusion pressure.

Moreover, at a given shear rate, the viscosity decreases as temperature increases. This is mainly because elevated temperature enhances

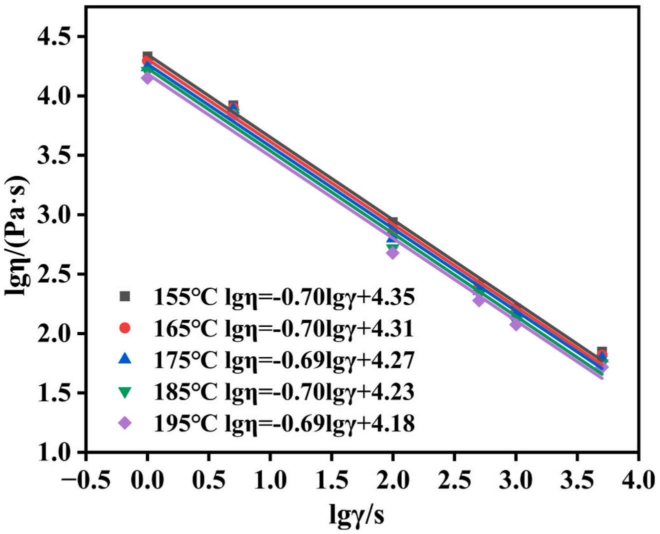

Fig. 2. Viscosity curves of mixtures at different nozzle temperatures.

the mobility of the binder phase, thereby reducing flow resistance and improving the flowability of the feedstock during extrusion. For pseudoplastic fluids, the relationship between shear viscosity and other parameters is demonstrated by Equation (2):

$$\eta = K\gamma^{n-1} \tag{2}$$

where η denotes the shear viscosity, γ is the shear rate, K and n represent the consistency index and flow behavior index, respectively. It is noted that $n < 1$ indicates shear-thinning behavior of the feedstock. Using linear fitting of the curves at each temperature shown in Fig. 2 (e.g., at 155 °C), the equation of $\lg \eta = -0.70 \lg \gamma + 4.35$ was formulated, and a relatively stable value of $n \approx 0.30$ was observed, confirming the pronounced shear-thinning characteristics of the feedstock. Meanwhile, the value of K slightly decreased with the increase of temperature, suggesting a general reduction in baseline melt viscosity. These results indicate that the shear rate primarily governs the instantaneous viscosity response, while temperature modulates the overall flow level. In summary, these two factors jointly influence the rheological behavior of the melt near the nozzle region.

To evaluate the printability of the developed feedstock, a series of unsupported structures with varying inclination angles (the constant height of 25 mm was maintained) were fabricated, as shown in Fig. 3. When the inclination angle was less than 150°, the structures exhibited stable formation without noticeable deformation or interlayer defects, indicating good shape retention capability. However, at an inclination angle of 150°, deformation and defects were observed on the overhanging regions due to the reduced interlayer contact area and the effect of gravity. These results suggest that the feedstock and printing process are suitable for fabricating complex ceramic components with features, such as inclined surfaces and overhanging geometries.

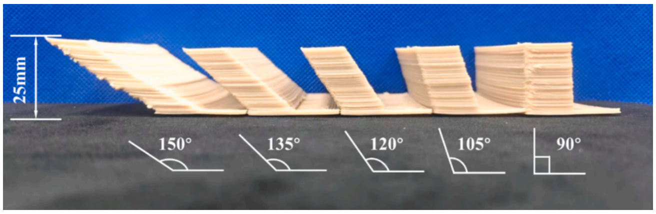

Fig. 3. Unsupported structures with different inclinations.

3.2. Single-factor screening for feasible process windows

To reasonably determine the experimental ranges of the process parameters, single-factor analyses of four key parameters, including the nozzle temperature (T), layer height (H), extrusion flow rate (Q), and printing speed (V), were initially conducted by maintaining the other parameters constant. The specimens were hollow cubes with dimensions of 40 mm × 40 mm × 40 mm. The design of the experiment for sampling points is provided in Table 1, while the corresponding macroscopic appearances and micrographs are shown in Figs. 4 and 5, respectively. The deposition continuity, surface quality, and interlayer bonding of the specimens were evaluated both macroscopically and microscopically, enabling the reliable determination of feasible bounds of each factor, and therefore providing a reference to parameter bounds used in subsequent multi-factor experiments.

Considering that the softening point of the particulate feedstock is approximately 140 °C and the thermal decomposition temperature of the EVA component is around 230 °C, four representative nozzle temperatures of 155, 175, 195, and 205 °C are selected for the printing tests, while keeping the other three parameters constant. For nozzle temperatures at 155 and 175 °C, the specimens exhibited behaviors such as smooth surfaces, continuous deposition lines, and good interlayer bonding. At 195 °C, slight local material accumulation was observed, but the overall quality remained acceptable. However, the excessive melt flow at 205 °C spread along the contour, causing noticeable accumulation and bulging, leading to reduced forming quality. Therefore, the experimental test at 205 °C was excluded, and three values of 155, 175, and 195 °C were considered suitable nozzle temperatures.

The layer height is generally set to no more than half of the nozzle diameter, and four levels of 0.15, 0.25, 0.35, and 0.45 mm were initially considered. At the layer height of 0.15 mm, over-extrusion occurred, resulting in the prolonged printing time due to a significantly increased number of layers. For 0.25 and 0.35 mm, deposition was uniform with sufficient interlayer contact. However, results obtained at 0.45 mm indicated that insufficient contact between adjacent layers led to contour collapse and instability. Finally, the 0.15 and 0.45 mm were excluded in the tests, and 0.20 and 0.40 mm were used as the lower and upper bounds of the layer height.

As the extrusion flow rate determines the material supply per unit time, four levels of 70%, 90%, 110%, and 130% were selected on the basis of process experience. At the extrusion flow rate of 70%, deposition discontinuities and breaks were observed, but the lines were continuous and stable at 90% of the extrusion flow rate. It was noted that slight surface bulging appeared at the level of 110% and notably, excessive material accumulation caused severe surface bulging at 130%. To ensure line continuity and geometric accuracy, the range of 80% to 120% was determined as the lower and upper bounds of the extrusion flow rate.

Furthermore, the printing speed affects both the residence time of the melt in the nozzle and the cooling process. Taking equipment stability and the rated speed limits into account, four levels of 20, 30, 40, and 50 mm/s were adopted. At 20 mm/s, the deposition was sufficient and the interlayer bonded tightly, but efficiency was low. At 30 mm/s, deposition and bonding remained adequate with higher efficiency. While at 40 and 50 mm/s, insufficient melt cooling and the reduced

Table 1
Experimental settings for single-factor analysis.

Parameters	Test Levels	Fixed Levels
T(°C)	155(T1), 175(T2), 195(T3), 205 (T4)	H = 0.15 mm, Q = 100%, V = 30 mm/s
H(mm)	0.15(H1), 0.25(H2), 0.35(H3), 0.45(H4)	T = 175 °C, Q = 100%, V = 30 mm/s
Q(%)	70(Q1), 90(Q2), 110(Q3), 130 (Q4)	H = 0.35 mm, T = 155 °C, V = 30 mm/s
V(mm/s)	20(V1), 30(V2), 40(V3), 50(V4)	H = 0.25 mm, T = 175 °C, Q = 100%

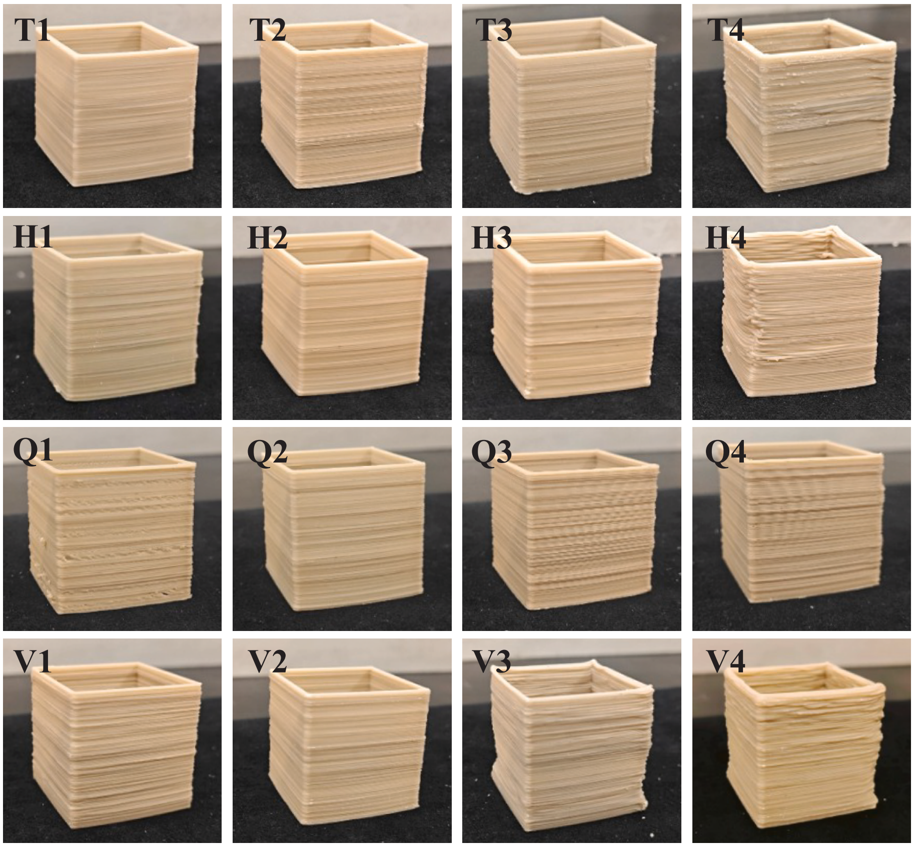

Fig. 4. Macroscopic morphology of printed green bodies with different process parameters. (For interpretation of the references to colour in this figure legend, the reader is referred to the web version of this article.)

motion stability were observed, leading to local contour instability and deposition deformation. Based on the forming quality and efficiency, the range of 25–45 mm/s was selected as the bound of the printing speed.

In summary, through single-factor screening tests, a feasible process window was determined with the nozzle temperature, layer height, extrusion flow rate, and printing speed ranging from 155 to 195 °C, 0.20 to 0.40 mm, 80% to 120%, and 25 to 45 mm/s, respectively. This provides a useful insight into the optimal ranges of design parameters for the subsequent multi-factor experimental design by the neural network model.

3.3. Effect of process parameters on planar dimensional deviation

The external quality of green bodies produced by ceramic FDM strongly influences the final performance of components. Planar dimensional deviation serves as a measurable indicator of the uniformity of layer deposition, surface roughness, and latent structural flaws, thus reflecting the external integrity and functional reliability of the part [32,33]. Large deviations arising from the printing process often trigger instabilities in the deposition stage or uneven material distribution, which is likely to be magnified in the debinding and sintering stages, resulting in internal porosity and crack formation [34]. Taking this fact into account, the planar dimensional deviation was used as a metric to evaluate the external quality of green bodies in this section, enabling an efficient preliminary appraisal of overall forming quality. To investigate the influence of process parameters on planar dimensional deviation during FDM, four key parameters – H, Q, T, and V- were defined as design variables. The bounds and levels for these four variables were determined based on the results of single-factor experiments in Section 3.2, and a total of 40 experimental runs were generated using the LHS method. The complete sampling matrix is provided in Table S1 of the Supplementary material.

Using the data in Table S1, a PDD-ANN model was constructed to predict planar dimensional deviation based on the process parameters, as shown in Fig. 6. The input layer consists of 4 nodes, corresponding to the four process parameters and the first hidden layer contains 10 neurons, while the second hidden layer contains 4 neurons and the output layer has a single node for regression prediction of dimensional deviation. All hidden layers employ the Swish activation function, which has demonstrated good smoothness and gradient stability for nonlinear regression tasks. The dataset was split into training and validation sets at an 80:20 ratio to ensure good fitting and predictive accuracy of the model. After the training process, the entire parameter space represented by 4 factors at 5 levels (a total of 625 combinations) was used to constrain a comprehensive dimensional deviation response surface for the prediction of the corresponding error values. Using this approximation model, systematic parameter sensitivity and interaction analysis were performed to provide theoretical support and subsequent parameter selection for improved mechanical performance of the printed parts. This approach significantly enhances the systematic nature of the ceramic FDM process throughout an effective sampling scheme while reducing the experimental workload.

Fig. 7 shows the results on the training set, validation set, and the entire dataset during the regression analysis, respectively. The solid line represents the linear fit, while the dashed line represents the ideal fit on the ground data. As the fitted curve almost overlaps the ideal fitting, the R^2 value for the entire dataset is 0.9854 and close to 1, indicating that the ANN model demonstrates excellent prediction performance in the design space, with a high correlation between the predicted and experimental values.

Moreover, the relative feature weights of four process parameters on the planar dimensional deviation and the interaction strengths between

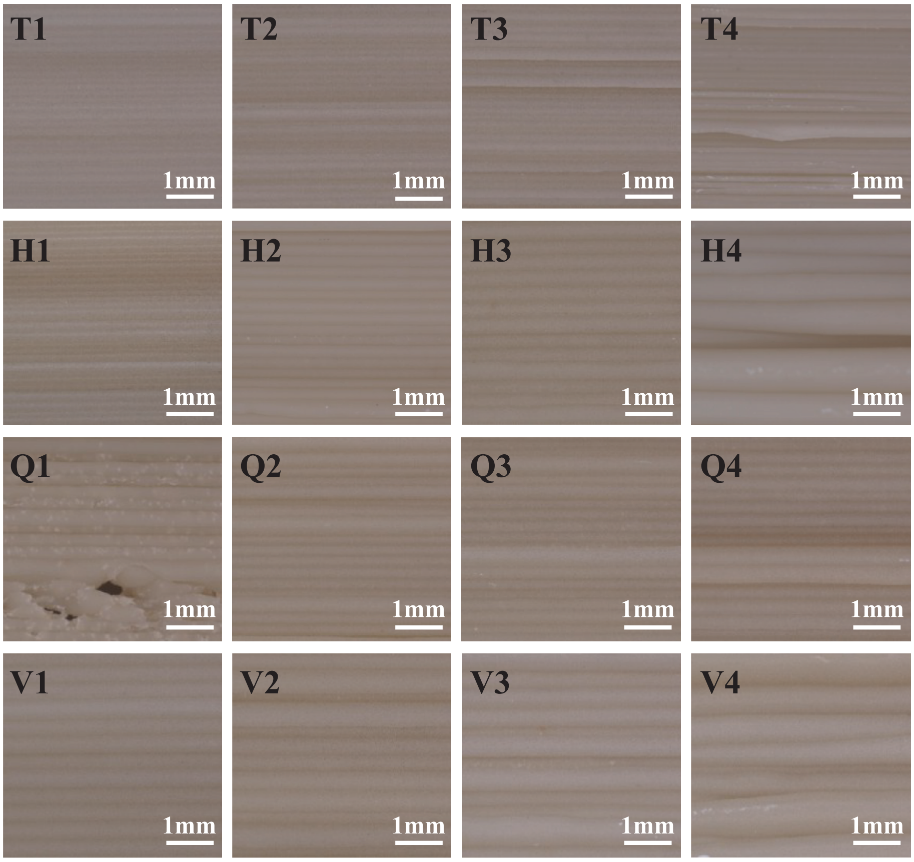

Fig. 5. Surface morphology of printed green bodies under different process parameters observed by ultra-depth optical microscopy. (For interpretation of the references to colour in this figure legend, the reader is referred to the web version of this article.)

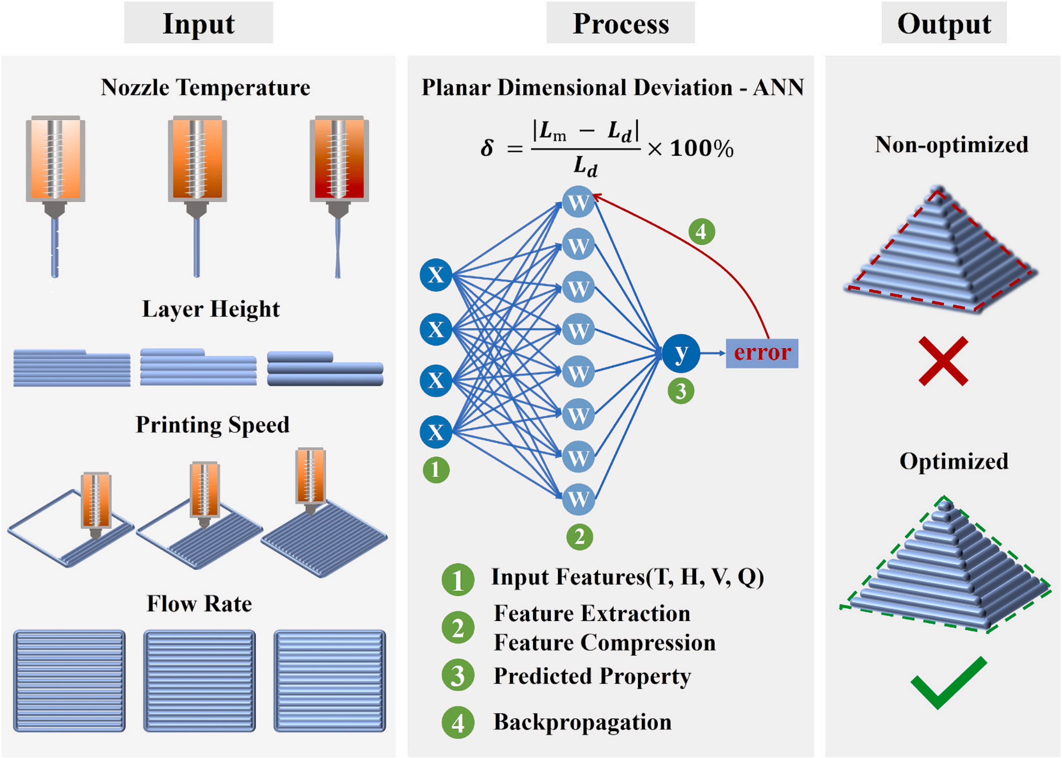

Fig. 6. Schematic of the PDD-ANN architecture (4-10-4-1).

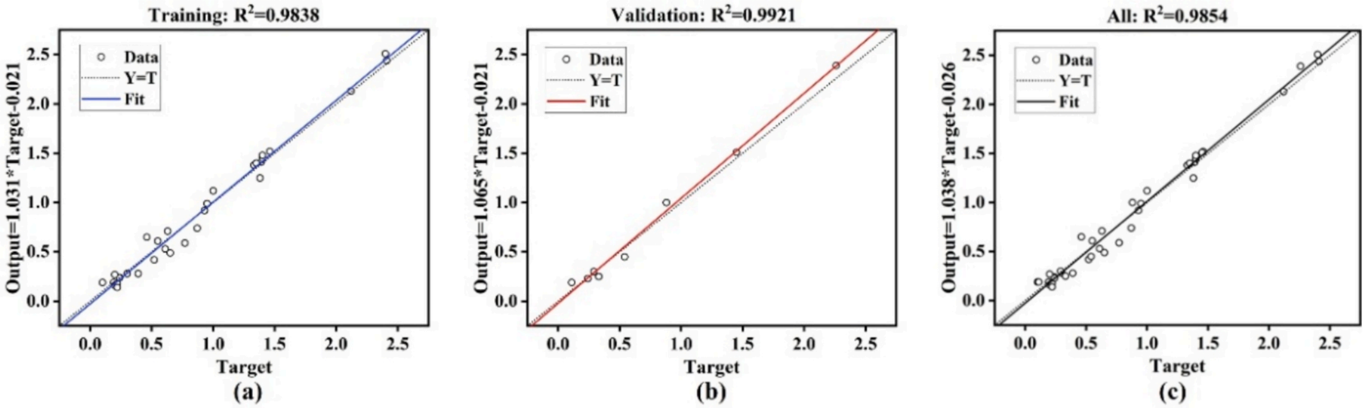

Fig. 7. Correlation coefficient of dimensional deviation data in the neural network.

parameters were investigated. Fig. 8 shows that H (41.8%), T (39.0%), V (12.1%), and Q (7.1%) are the main influencing factors in descending order. Among these factors, the layer height (H) plays a dominant role in line deposition and interlayer bonding. Reducing the layer height improves the formation resolution, but excessive reduction can lead to over-deposition and cause contour bulging. Increasing the layer height enhances the printing efficiency, while this could weaken the interlayer bonding strength and result in formation distortion. The nozzle temperature (T) ranks second, directly affecting the melt flowability and interlayer adhesion. Excessively high temperatures cause over-flowing of the melt and edge bulging, and low temperatures reduce flowability and can lead to deposition defects. The printing speed (V) and extrusion flow rate (Q) have relatively slighter effects, but proper adjustment of these two parameters can improve the thermal management and balance deposition, thereby enhancing overall print quality.

Fig. 9a shows the interaction effect between process parameters, ranked as follows: T × H (1.000), T × Q (0.740), T × V (0.690), H × V (0.410), H × Q (0.350), and Q × V (0.070), where × represents the interaction effect. Among these, the last three correlation coefficients are relatively small and the strength of the relationship can be considered negligible. Fig. 9b shows that the dimensional deviation exhibits a trend of decrease and then turns into an increase with changes in the layer height and temperature. It is noted that the better ranges of the layer height and nozzle temperature should be defined as 0.20–0.30 mm and 155–175 °C, respectively. With these ranges, the melt flowability and interlayer bonding are balanced, leading to minimized errors. Moreover, a clear inverse coupling between extrusion flow rate and nozzle temperature is observed in Fig. 9c. At low temperatures (≤175 °C), increasing the flow rate effectively reduces the error; however, at high temperatures (>175 °C), an excessive flow rate causes the melt overflow and edge piling, which amplify the error. Therefore, the parameter combination of high-temperature and high-flow rate or low-temperature and low-flow rate should be avoided. Fig. 9d reveals that the dimensional deviation increases with the printing speed, and this trend is further amplified at higher temperatures. Under conditions of 155–165 °C and the printing speed of 25–35 mm/s, a good deposition match and minimal error can be achieved.

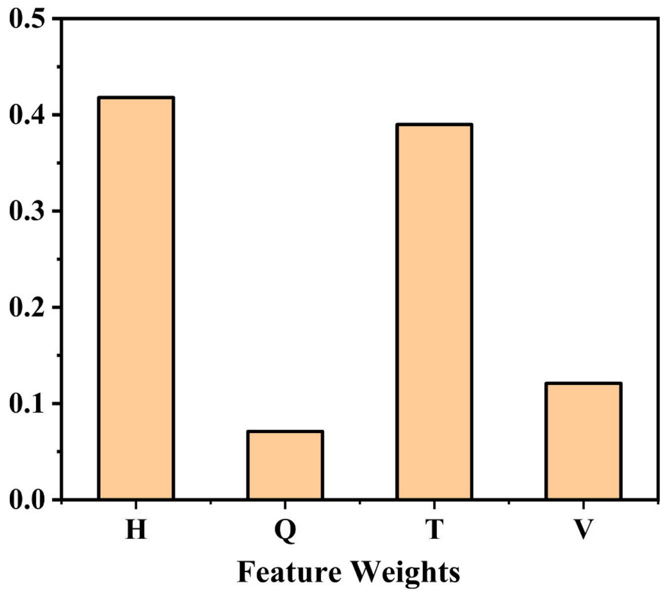

Fig. 8. Relative feature weights of H, Q, T, and V.

Based on the above analysis, the parameter ranges for minimizing planar dimensional deviation (less than 0.2%) were determined by a full factorial combination analysis as follows: T, H, V, and Q range from 155 to 175 °C, 0.20 to 0.30 mm, 25 to 45 mm/s, and 80 to 120%, respectively. These ranges will be applied to the flexural strength experiments in the following section to improve efficiency and reduce cost.

3.4. *Effect of process parameters on flexural strength*

The internal quality of ceramic FDM components is a critical factor determining their final mechanical performance and long-term reliability. Defects such as porosity, microcracks, and interlayer separation introduced during printing, debinding, and sintering significantly degrade the densification behavior and weaken the overall structural integrity [9,35]. The three-point bending strength serves as a quantitative indicator that indirectly reflects the presence and severity of such defects. Therefore, this section evaluates the internal quality of the sintered components using three-point bending strength, providing a reliable basis for process optimization and performance enhancement. To further establish the quantitative relationship between process parameters and flexural strength, this section focused on the construction of a FS-ANN model for the accurate prediction of flexural strength. The model retained the basic framework used in Section 3.3, and more developments were implemented as follows: the number of input nodes was adapted from four (H, Q, T, V) to three (H, T, V) to decrease experimental workload. Also, considering the natural distribution of flexural strength data, hyperparameters such as regularization coefficients, dropout rate, and learning rate were reconfigured to speed up the network convergence. A total of 30 experimental runs were generated using the LHS method for the flexural strength study, and the complete sampling matrix is provided in Table S2 of the Supplementary material. After training, the mapping of input data over the entire three-factor, five-level parameter space (a total of 125 combinations) to the output of flexural strength was built to realize the accurate prediction of mechanical performances, providing useful guidance to subsequent

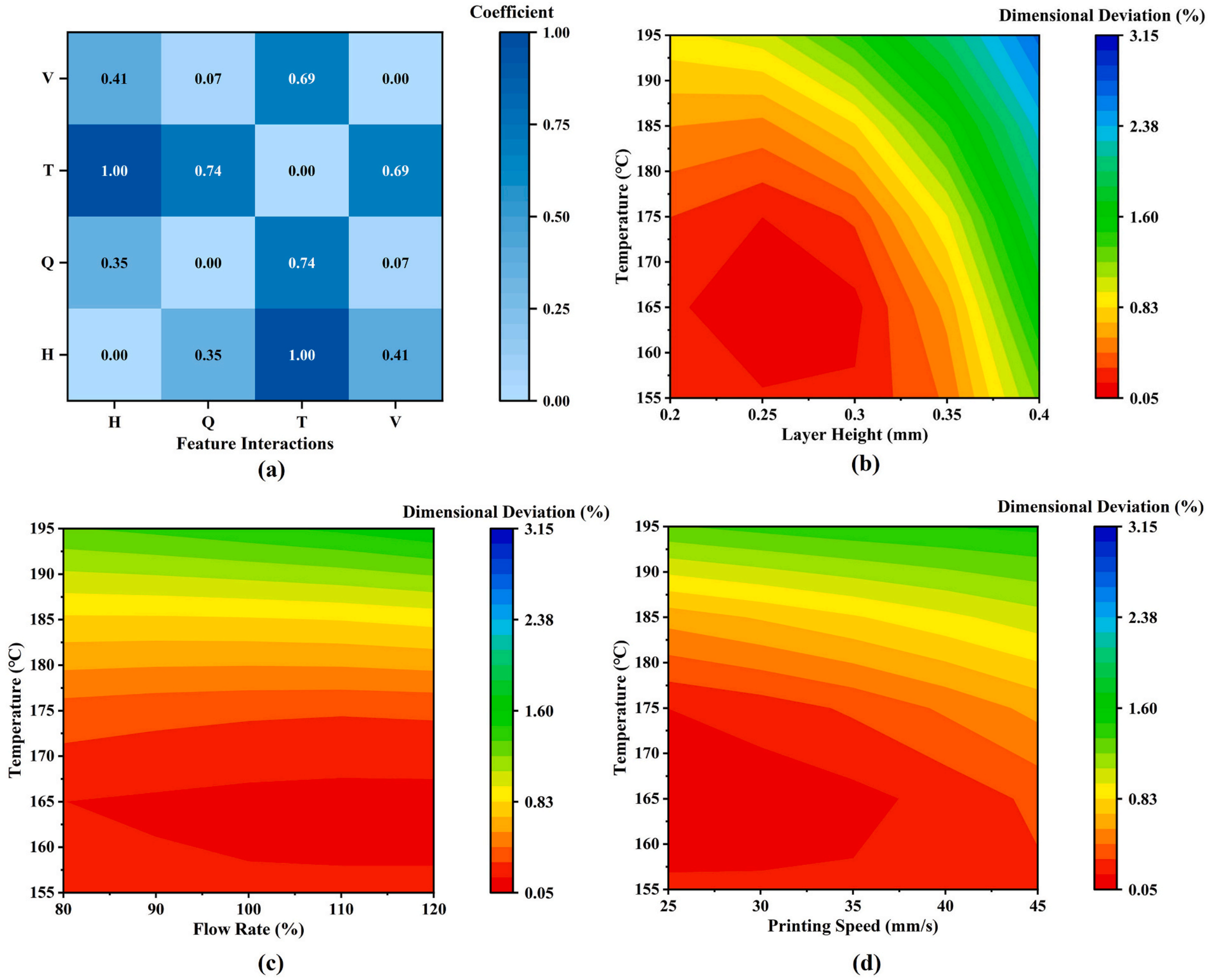

	H	Q	T	V
V	0.41	0.07	0.69	0.00
T	1.00	0.74	0.00	0.69
Q	0.35	0.00	0.74	0.07
H	0.00	0.35	1.00	0.41

Fig. 9. Correlation analysis and contour mapping of dimensional deviation: (a) Interaction matrix between parameters H, Q, T, V, (b-d) Interactive effects of the nozzle temperature, layer height, flow rate, and printing speed on dimensional deviation.

parameter optimization and experimental validation.

Fig. 10 shows that as the fitted curve almost overlaps the ideal line, the R^2 value (0.9857) for the entire dataset is close to 1, indicating that the ANN model demonstrates great accuracy in predicting structural flexural strength and a significant linear correlation between the predicted and experimental values.

To investigate interaction weights of each process parameter on flexural strength, the corresponding feature weights are provided in Fig. 11. It is noted that H (60.7%), V (20.9%), and T (18.4%) are the main influencing factors ranked in descending order.

Feature importance analysis reveals that the layer height (H) occupies the highest weight among the three process variables, significantly surpassing printing speed and nozzle temperature. To validate this conclusion from a structural perspective and analyze the underlying mechanism, cross-sectional microstructural characterization was performed on representative sintered samples selected from the LHS design (Fig. 12). Specifically, three representative samples with low (H = 0.18 mm), intermediate (H = 0.22 mm), and high (H = 0.34 mm) layer heights were selected for comparison. Their corresponding sampling numbers and full processing parameters are provided in Table S2 of the

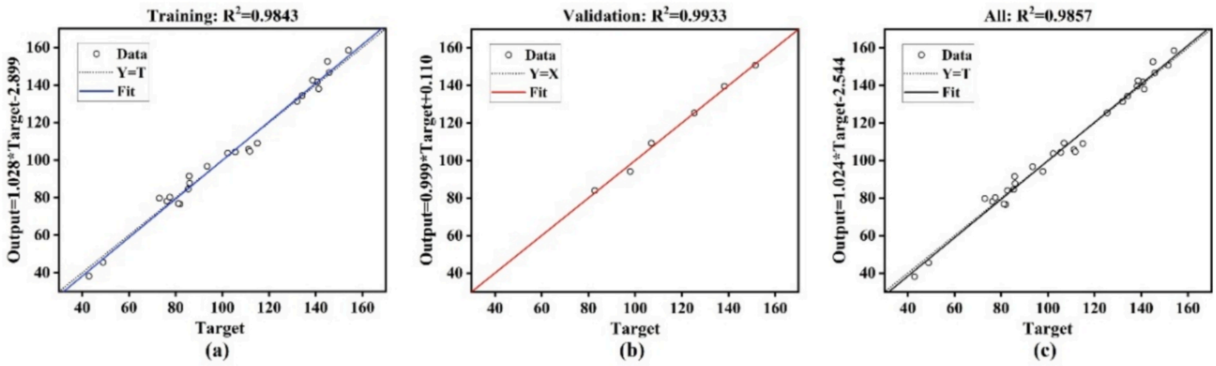

Fig. 10. Correlation coefficient of flexural strength data in the neural network.

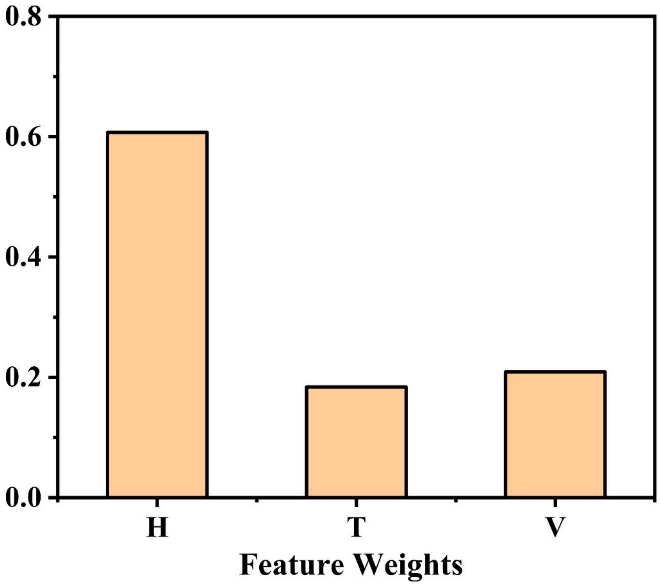

Fig. 11. Relative feature weights of H, T, and V.

Supplementary material. As shown in Fig. 12a and d, at H = 0.18 mm, discontinuous cracks appeared in the cross-section. These cracks were not distributed in parallel to the layer interface, but exhibited a distinct inclined and deflected morphology. This phenomenon is attributed to the reduced deposition gap under excessively low layer height conditions, which leads to the nozzle exerting strong compaction and tangential dragging effects on the deposited layer. This introduces local structural inhomogeneity within the green body, which is subsequently amplified during the sintering process. When H was 0.22 mm (Fig. 12b and e), the cross-sectional structure was relatively dense with continuous interlayer bonding, and no obvious macroscopic defects were observed. In contrast, when H was increased to 0.34 mm (Fig. 12c and f), large triangular voids formed between adjacent deposited filaments, constituting macroscopic structural defects between layers. Such defects reduce the effective load-bearing area and may act as stress concentration regions under bending loads. Overall, variations in H regulate the structural integrity of the sintered body by influencing interlayer geometric matching and initial defect morphology, consistent with its dominant role identified in the feature importance analysis.

Following that, the printing speed ranks second: a moderate speed helps maintain a balance among melting, deposition, and cooling, therefore improving the bonding quality. Excessive speed can lead to interface defects, while a speed that is too slow can cause heat accumulation and induce thermal stress. Thus, a trade-off analysis between strength and manufacturing efficiency should be considered to balance the requirements. The nozzle temperature has a relatively smaller impact, as its range is narrow. Thus, an appropriate temperature ensures better melt flowability, thereby enhancing interlayer adhesion.

Fig. 13a shows the interaction strengths between process parameters and their impact on flexural strength, ranked from high to low as follows: H × V (0.970), T × V (0.820), and H × T (0.720). Fig. 13b indicates that the flexural strength reaches its peak within the combination of the H (0.20–0.24 mm) and V (25–40 mm/s), presenting the optimal matching window. In these ranges, the melt deposition rate and layer thickness match well, which favors stable material deposition and sufficient interlayer overlap, thereby reducing internal void formation and improving interlayer bonding. However, a sharp strength decline is observed in the high-H region, implying that the reduced overlap area weakens the structural integrity. Fig. 13c shows the flexural strength peaks within the temperature range of 155 to 170 °C and speed range of 20 to 25 mm/s, demonstrating that the material's flowability and interfacial adhesion are well-balanced. The contour gradient reveals that the excessive speed (>35 mm/s) coupled with high temperature leads to a strength reduction, which may be related to excessive melt flowability and insufficient deposition stability under high-speed conditions, thereby hindering the formation of a dense and well-bonded structure. Fig. 13d shows that within the lower to intermediate layer height range, the flexural strength initially increases with the temperature and then decreases, indicating the existence of an optimal matching window. Notably, the contour map indicates that the increasing temperature cannot compensate for the strength loss at large layer heights (>0.30 mm), suggesting that geometric defects dominate over thermally enhanced interlayer bonding. Within this window, the layer height and nozzle temperature synergistically ensure adequate melt flow and stable deposition, effectively reducing thermal stress and formation defects, thereby enhancing the structural density and flexural strength.

Based on the above analysis, the parameter range for achieving a flexural strength greater than 150 MPa was determined using the full factorial combination analysis as follows: For better flexural strength, T, H, and V should vary in the range of 155 to 170 °C, 0.22 to 0.26 mm, and 20 to 40 mm/s, respectively. Within these ranges, the synergistic effect of the process parameters contributes to achieving better deposition quality and interlayer bonding, significantly improving the structural

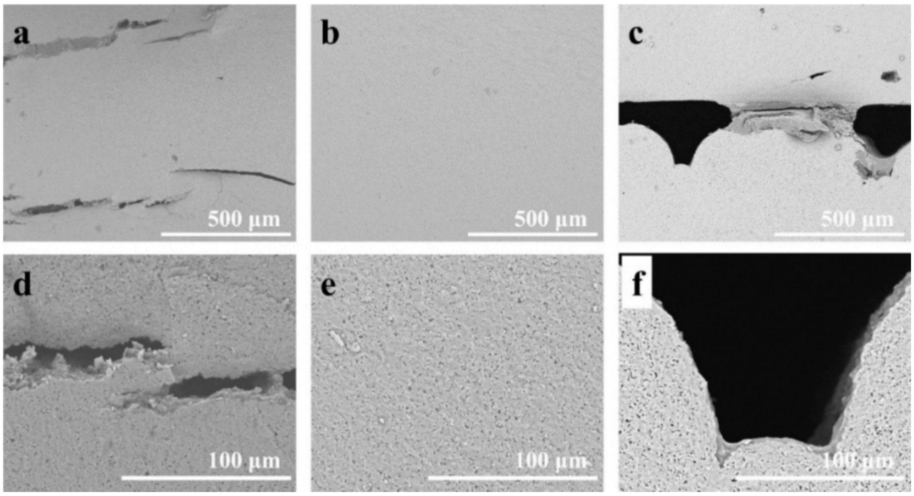

Fig. 12. Cross-sectional SEM micrographs of sintered samples selected from the LHS design. (a, d) Sample 28 (H = 0.18 mm), (b, e) Sample 9 (H = 0.22 mm), (c, f) Sample 5 (H = 0.34 mm).

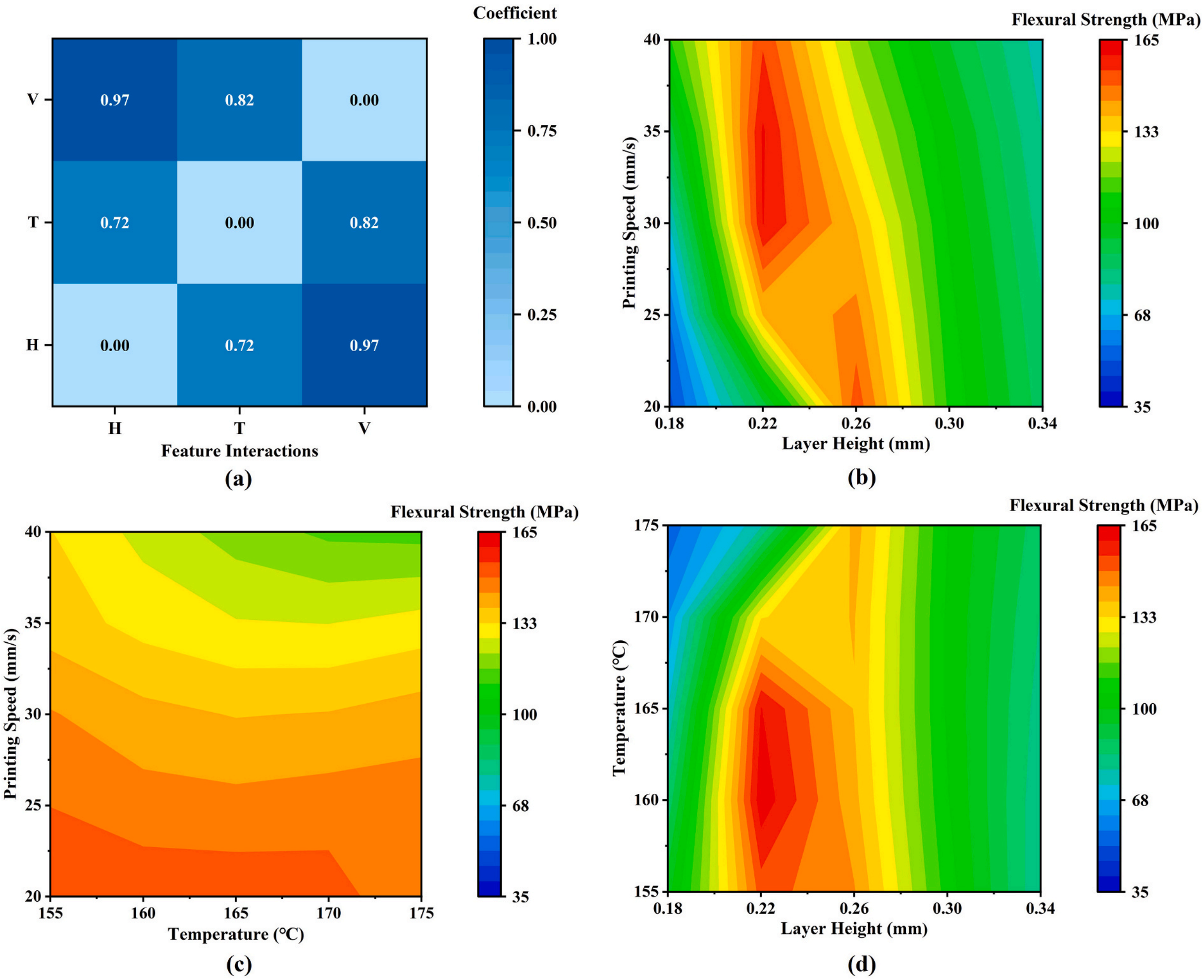

Fig. 13. Correlation analysis and contour mapping of flexural strength: (a) Interaction matrix between parameters H, T, and V, (b-d) Interactive effects of the nozzle temperature, layer height, and printing speed on flexural strength.

density and mechanical properties. This is attributed to the fewer internal defects and a more uniform structure in the printed specimen, thereby laying a solid foundation for subsequent sintering.

3.5. Experimental validation of the optimal process parameters

All updated bounds of parameters, including layer height (H), nozzle temperature (T), and printing speed (V), were used to generate full factorial input data, while maintaining the original number of levels. These inputs were then fed into the aforementioned PDD-ANN model to predict dimensional deviations, with the extrusion flow rate (Q) fixed at 100%. The ANN-based prediction results for all candidate optimal parameter sets are provided in Table S3 of the Supplementary material. All selected parameter combinations yielded predicted dimensional deviations below 0.23%, confirming the effectiveness of the two-stage modeling strategy. Furthermore, the parameter set with the highest predicted flexural strength (T = 160 °C, H = 0.22 mm, V = 30 mm/s) was selected as the final optimal combination for printing experiments. To validate the accuracy of the model predictions and the applicability of the process, comprehensive experimental evaluations of the printed specimens were conducted from the dimensional deviation and flexural strength perspectives.

In terms of dimensional deviation, the measured error was 0.24%, slightly higher than the predicted value of 0.21%, but still within the acceptable tolerance, verifying the predictive accuracy and reliability of the developed PDD-ANN model within the experimental domain. As shown in Fig. 14a and b, the specimens fabricated using the optimal parameters exhibited clear edges and relatively flat deposition, with minimal over-deposition or collapse. The overall appearance was significantly superior to the specimens printed with the non-optimized parameters. In terms of mechanical properties, the flexural strength of the sintered specimens was 155.8 MPa, showing a deviation of 4.5% from the predicted value of 163.2 MPa, validating the applicability and reliability of the FS-ANN model.

In order to fabricate fully dense cordierite ceramics, the printed ceramics with optimal processing condition were further post-HIP treated. After HIP treatment at 1310 °C for 2 h with argon gas pressure of 130 MPa, translucent ceramics with a sintered density of 2.51 g/cm^3 (corresponding to a relative density of 99.4%) were achieved, shown in Fig. 14c. It can be observed that the post-heat-treated samples demonstrated good interlayer bonding with no defects or printing marks. Furthermore, the SEM image of the fracture surface in Fig. 14d supports the conclusion of tight interlayer fusion and minimal internal porosity, indicating that the optimized parameter combination effectively improves the structural density and mechanical properties.

After the HIP process, the flexural strength was increased to 196.8 MPa, which approaches the level of conventionally dry-pressed specimens (200 MPa). This strength enhancement is further supported by the statistical analysis, with a Weibull modulus of 8.95 and a characteristic strength of 207.3 MPa (Fig. 15a). As summarized in Table 2, the mechanical properties are comparable to those reported for cordierite ceramics fabricated by other methods. Finally, such a set of parameters

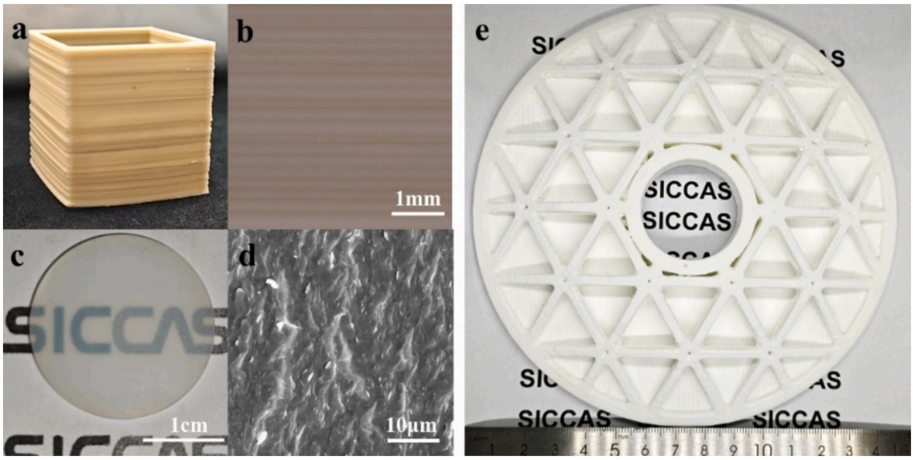

Fig. 14. FDM fabrication of cordierite ceramics with optimal parameters: (a), (b) Surface and structural morphology of the green body, (c) Image of 20 mm diameter sample after HIP, (d) SEM image of the fracture surface after HIP, (e) Cordierite reflector mirror with 148 mm diameter. (For interpretation of the references to colour in this figure legend, the reader is referred to the web version of this article.)

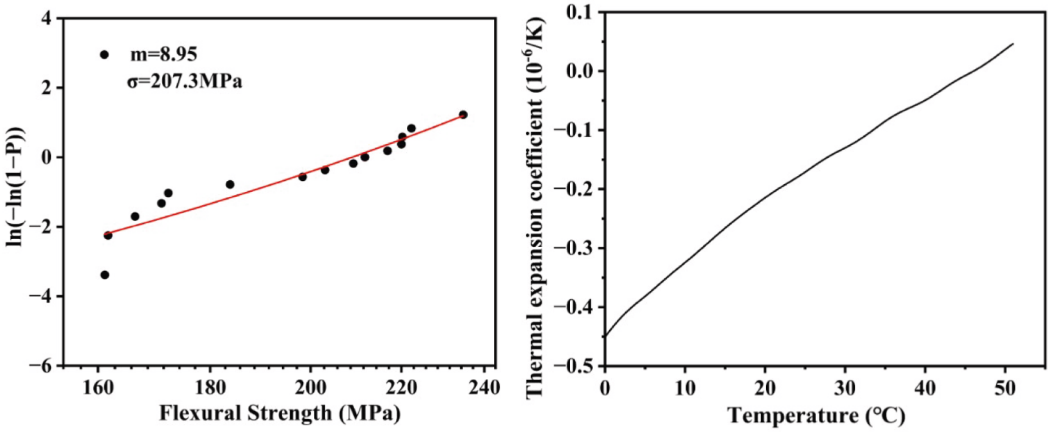

(a) (b)

Fig. 15. Characterization under optimized parameters: (a) Weibull modulus of flexural strength, (b) Thermal expansion coefficient curve.

Table 2
Comparison of the properties of cordierite ceramics in this work and others.

Fabrication method	Component Size (mm)	Density (g/cm^3)	Flexural Strength (MPa)	CTE ($10^{-6}/K$) at 22 °C	Ref.
FDM	148	2.51	197	−0.2	This work
DLP	50	2.51	207	−0.2	[12]
DLP	/	/	182	/	[36]
DIW	/	2.37	24	1.69	[37]
Dry Pressing	500	2.54	200	0.02	CO720[a]

[a] https://www.kyocera.com.cn/prdct/fc/product/pdf/material.pdf

were determined to print a 180 mm diameter cordierite ceramic mirror blank, which shrank to 148 mm after debinding and sintering, as shown in Fig. 14e. The fabricated cordierite ceramics exhibited excellent thermal stability: over the temperature range of 0–50 °C, the coefficient of thermal expansion (CTE) varied from approximately −0.45 to 0.05 × 10^{-6}/K in Fig. 15b.

In summary, the established ANN-based PDD-ANN and FS-ANN models with the integration of the sampling strategy demonstrate excellent performance of the printed cordierite components by experimental validations, achieving a good balance between dimensional accuracy and flexural strength. This provides a feasible pathway to the optimal design of ceramic FDM for cordierite components in the complex printing process.

4. Conclusion

In this study, a systematic and data-driven framework applied to cordierite ceramic fabrication by FDM has been successfully developed with the integration of stepwise experimental screening and artificial neural network models, enabling efficient parameter optimization and intelligent computation features.

First, four key parameters – the nozzle temperature (T), layer height (H), printing speed (V), and extrusion flow rate (Q) – have been identified to effectively affect the external quality of the green bodies and their nonlinear coupling behaviors using the PDD-ANN model. To minimize the planar dimensional deviation (<0.23%), the parameter ranges have been determined by a full factorial analysis as follows: T, H, V, and Q in the range of 155 to 175 °C, 0.20 to 0.30 mm, 25 to 45 mm/s, and 80 to 120%, respectively. As the extrusion flow rate has a limited influence on dimensional accuracy, it has been excluded from the following analysis.

Second, the FS-ANN model has been developed to elucidate three dominant factors that govern the internal quality of sintered ceramics and their coupling behaviors for maximizing flexural strength (>150 MPa). Crucially, microstructural characterization physically validated these data-driven findings, revealing that the layer height governs the mechanical performance by dictating the evolution of interlayer macroscopic defects. Thus, the above three parameters have been refined to 0.22 to 0.26 mm, 20 to 40 mm/s, and 155 to 170 °C, respectively.

Third, experimental verification using the optimal parameter combination has demonstrated green bodies with the predicted dimensional deviation of 0.21% and sintered bodies with the predicted flexural strength of 163.2 MPa, as compared with measured values of 0.24% and 155.8 MPa, respectively. These results have indicated a high level of agreement between model predictions and experimental tests, confirming the accuracy and reliability of the proposed framework.

Finally, a 180 mm-diameter cordierite ceramic mirror has been successfully fabricated, with a uniform shrinkage to 148 mm after debinding and sintering. The component has exhibited excellent dimensional stability and structural integrity, with no detectable warpage or cracks. These findings have conclusively verified the effectiveness and applicability of the proposed framework, establishing a systematic method for FDM fabrication of complex, high-performance cordierite ceramic components and providing both a feasible process route and theoretical foundation for their applications in high-end fields such as precision optics and aerospace.

CRediT authorship contribution statement

Pengxian Hui: Writing – original draft, Visualization, Methodology, Investigation, Formal analysis, Data curation, Conceptualization. **Haohao Ji:** Writing – review & editing, Supervision, Methodology, Investigation, Conceptualization. **Ye Ge:** Validation, Investigation, Data curation. **Jin Zhao:** Investigation, Formal analysis. **Wenlong Liu:** Resources, Investigation. **Shiwei Wang:** Writing – review & editing, Supervision, Methodology. **Dianzi Liu:** Writing – review & editing, Supervision, Methodology, Formal analysis. **Jian Zhang:** Writing – review & editing, Supervision, Resources, Project administration, Methodology, Investigation, Funding acquisition, Conceptualization.

Declaration of competing interest

The authors declare that they have no known competing financial interests or personal relationships that could have appeared to influence the work reported in this paper.

Acknowledgements

This work was supported by National Natural Science Foundation of China (Grant No. 62405345). The author would like to thank eceshi (www.eceshi.com) for rheological analysis.

Appendix A. Supplementary data

Supplementary data to this article can be found online at https://doi.org/10.1016/j.matdes.2026.115993.

Data availability

The data that support the findings of this study are available from the corresponding author upon reasonable request.

References

[1] O. Khomenko, A. Zaichuk, A. Amelina, Low-temperature cordierite ceramics with porous structure for thermal shock resistance products, Open Ceram. 17 (2024) 100520, https://doi.org/10.1016/j.oceram.2023.100520.

[2] H. Gökçe, D. Ağaoğulları, M.L. Öveçoğlu, İ. Duman, T. Boyraz, Characterization of microstructural and thermal properties of steatite/cordierite ceramics prepared by using natural raw materials, J. Eur. Ceram. Soc. 31 (2011) 2741–2747, https://doi.org/10.1016/j.jeurceramsoc.2010.12.007.

[3] Y. Guo, Y. Ge, W. Liu, J. Zhao, J. Zhang, S. Wang, Reactive-sintered low-thermal-expansion cordierite ceramic with high stiffness, J. Ceram. Sci. Technol. (2024), https://doi.org/10.4416/JCST2024-00003.

[4] T. Kamiya, T. Mizutani, Development of ultra-lightweight and thermally-stable cordierite ceramic mirrors, in: R. Geyl, R. Navarro (Eds.), SPIE, Austin, United States, 2018: p. 23. doi:10.1117/12.2313073.

[5] D.-E. Hyun, J.-B. Jeon, Y.-S. Lee, Y.-N. Kim, M. Kim, S. Ko, S.-M. Koo, W.H. Shin, C. Park, D.-W. Lee, J.-M. Oh, Fabrication of large-area mullite–cordierite composite substrates for semiconductor probe cards and enhancement of their reliability, Materials 15 (2022) 4283, https://doi.org/10.3390/ma15124283.

[6] M. Terada, K. Kawamura, I. Kagomiya, K. Kakimoto, H. Ohsato, Effect of ni substitution on the microwave dielectric properties of cordierite, J. Eur. Ceram. Soc. 27 (2007) 3045–3048, https://doi.org/10.1016/j.jeurceramsoc.2006.11.050.

[7] C. Zou, Y. Xiao, L. Li, J. Chen, W. Sun, X. Guo, Preparation of high-purity silicon carbide ceramics by hot pressing sintering, Nanomaterials 15 (2025) 825, https://doi.org/10.3390/nano15110825.

[8] H. Chen, S. Shimai, J. Zhao, Z. Di, X. Mao, J. Zhang, J. Liu, G. Zhou, S. Wang, Pressure filtration assisted gel casting in translucent alumina ceramics fabrication, Ceram. Int. 44 (2018) 16572–16576, https://doi.org/10.1016/j.ceramint.2018.06.079.

[9] Z. Chen, Z. Li, J. Li, C. Liu, C. Lao, Y. Fu, C. Liu, Y. Li, P. Wang, Y. He, 3D printing of ceramics: a review, J. Eur. Ceram. Soc. 39 (2019) 661–687, https://doi.org/10.1016/j.jeurceramsoc.2018.11.013.

[10] Y. Yang, Delay optimisation of gradient-doped nd: YAG laser ceramics via active mixing of direct ink writing, (2025).

[11] Z. Chen, C. Liu, J. Li, J. Zhu, Y. Liu, C. Lao, J. Feng, M. Jiang, C. Liu, P. Wang, Y. Li, Mechanical properties and microstructures of 3D printed bulk cordierite parts, Ceram. Int. 45 (2019) 19257–19267, https://doi.org/10.1016/j.ceramint.2019.06.174.

[12] Y. Tai, H. Ji, T. Ma, J. Zhao, J. Zhang, S. Wang, Fabrication of dense cordierite ceramics with high mechanical properties via interlayer defect-free digital light processing (DLP), Ceram. Int. (2025) S0272884225016426, https://doi.org/10.1016/j.ceramint.2025.04.031.

[13] S. Huang, C. Ye, H. Zhao, Z. Fan, Additive manufacturing of thin alumina ceramic cores using binder-jetting, Addit. Manuf. 29 (2019) 100802, https://doi.org/10.1016/j.addma.2019.100802.

[14] A. Ur Rehman, A. Ullah, T. Liu, R. Ur Rehman, M.U. Salamci, Additive manufacturing of Al2O3 ceramics with MgO/SiC contents by laser powder bed fusion process, Front. Chem. 11 (2023) 1034473, https://doi.org/10.3389/fchem.2023.1034473.

[15] S. Bose, E.K. Akdogan, V.K. Balla, S. Ciliveri, P. Colombo, G. Franchin, N. Ku, P. Kushram, F. Niu, J. Pelz, A. Rosenberger, A. Safari, Z. Seeley, R.W. Trice, L. Vargas-Gonzalez, J.P. Youngblood, A. Bandyopadhyay, 3D printing of ceramics Advantages, challenges, applications, and perspectives, J. Am. Ceram. Soc. (2024) jace.20043, https://doi.org/10.1111/jace.20043.

[16] F.-F. Li, N.-N. Ma, J. Chen, M. Zhu, W.-H. Chen, C.-C. Huang, Z.-R. Huang, SiC ceramic mirror fabricated by additive manufacturing with material extrusion and laser cladding, Addit. Manuf. 58 (2022) 102994, https://doi.org/10.1016/j.addma.2022.102994.

[17] T. Shen, H. Xiong, Z. Li, L. Zhang, K. Zhou, Additive manufacturing of dense zirconia ceramics by fused deposition modeling via screw extrusion, Ceram. Int. 47 (2021) 34352–34360, https://doi.org/10.1016/j.ceramint.2021.08.348.

[18] B. Vijay, R. Nidagundi, C.P.S.P. Keshavamurthy, Studies on parametric optimization for fused deposition modelling process, Mater. Today: Proc. 2 (2015) 1691–1699, https://doi.org/10.1016/j.matpr.2015.07.097.

[19] A. Dey, N. Yodo, A systematic survey of FDM process parameter optimization and their influence on part characteristics, (n.d.). doi:10.3390/jmmp3030064.

[20] A. Panico, A. Corvi, L. Collini, C. Sciancalepore, Multi objective optimization of FDM 3D printing parameters set via design of experiments and machine learning algorithms, Sci. Rep. 15 (2025), https://doi.org/10.1038/s41598-025-01016-z.

[21] R. Spina, L. Morfini, Material extrusion additive manufacturing of ceramics: a review on filament-based process, Materials 17 (2024) 2779, https://doi.org/10.3390/ma17112779.

[22] S. Deswal, R. Narang, D. Chhabra, Modeling and parametric optimization of FDM 3D printing process using hybrid techniques for enhancing dimensional preciseness, Int. J. Interact. Des. Manuf. (ijidem) 13 (2019) 1197–1214, https://doi.org/10.1007/s12008-019-00536-z.

[23] Y. Li, F. Ding, W. Tian, Optimization of 3D printing parameters on deformation by BP neural network algorithm, Metals 12 (2022) 1559, https://doi.org/10.3390/met12101559.

[24] L. Deng, B. Feng, Y. Zhang, An optimization method for multi-objective and multi-factor designing of a ceramic slurry: Combining orthogonal experimental design with artificial neural networks, Ceram. Int. 44 (2018) 15918–15923, https://doi.org/10.1016/j.ceramint.2018.06.010.

[25] R.M.D. Andrade, A.C. Eduardo, Methodology for automatic process of the fired ceramic tile's internal defect using IR images and artificial neural network, J. Braz. Soc. Mech. Sci. & Eng. 33 (2011) 67–73, https://doi.org/10.1590/S1678-58782011000100010.

[26] D.J. Scott, P.V. Coveney, J.A. Kilner, J.C.H. Rossiny, N.M.N. Alford, Prediction of the functional properties of ceramic materials from composition using artificial neural networks, J. Eur. Ceram. Soc. 27 (2007) 4425–4435, https://doi.org/10.1016/j.jeurceramsoc.2007.02.212.

[27] K. Lu, X. Chen, J. Zhang, J. Chen, Z. Liu, L. Chen, Comparison of artificial neural network and response surface methodology prediction in key performance of two-component grout material in shield tunneling, Case Stud. Constr. Mater. 23 (2025) e05020, https://doi.org/10.1016/j.cscm.2025.e05020.

[28] L. Meng, B. McWilliams, W. Jarosinski, H.-Y. Park, Y.-G. Jung, J. Lee, J. Zhang, Machine learning in additive manufacturing: a review, JOM 72 (2020) 2363–2377, https://doi.org/10.1007/s11837-020-04155-y.

[29] M.N. Morshed, M.N. Pervez, N. Behary, N. Bouazizi, J. Guan, V.A. Nierstrasz, Statistical modeling and optimization of heterogeneous fenton-like removal of organic pollutant using fibrous catalysts: a full factorial design, Sci. Rep. 10 (2020) 16133, https://doi.org/10.1038/s41598-020-72401-z.

[30] F. Hong, P. Wei, J. Fu, M. Beer, A sequential sampling-based bayesian numerical method for reliability-based design optimization, Reliab. Eng. Syst. Saf. 244 (2024) 109939, https://doi.org/10.1016/j.ress.2024.109939.

[31] P. Borisut, A. Nuchitprasittichai, Adaptive latin hypercube sampling for a surrogate-based optimization with artificial neural network, Processes 11 (2023) 3232, https://doi.org/10.3390/pr11113232.

[32] M.K. Thompson, G. Moroni, T. Vaneker, G. Fadel, R.I. Campbell, I. Gibson, A. Bernard, J. Schulz, P. Graf, B. Ahuja, F. Martina, Design for additive manufacturing: Trends, opportunities, considerations, and constraints, CIRP Ann. 65 (2016) 737–760, https://doi.org/10.1016/j.cirp.2016.05.004.

[33] A. Karadag, O. Ulkir, Prediction of dimensional accuracy and surface quality in additively manufactured biomedical implants using ANN, Int. J. Precis. Eng. Manuf. 26 (2025) 1187–1213, https://doi.org/10.1007/s12541-025-01229-2.

[34] A. Zocca, P. Colombo, C.M. Gomes, J. Günster, Additive manufacturing of ceramics: issues, potentialities, and opportunities, J. Am. Ceram. Soc. 98 (2015) 1983–2001, https://doi.org/10.1111/jace.13700.

[35] N. Travitzky, A. Bonet, B. Dermeik, T. Fey, I. Filbert-Demut, L. Schlier, T. Schlordt, P. Greil, Additive manufacturing of ceramic-based materials, Adv. Eng. Mater. 16 (2014) 729–754, https://doi.org/10.1002/adem.201400097.

[36] W. Ren, W. Liu, X. Luo, Z. Liu, C. Liu, Z. Chen, 3D printing of cordierite glass-ceramics, Ceram. Int. 51 (2025) 1632–1642, https://doi.org/10.1016/j.ceramint.2024.11.139.

[37] Z. Chen, Z. Xu, F. Cui, J. Zhang, X. Sun, Y. Shang, R. Guo, N. Liu, S. Cai, C. Zheng, Direct ink writing of cordierite ceramics with low thermal expansion coefficient, J. Eur. Ceram. Soc. 42 (2022) 1685–1693, https://doi.org/10.1016/j.jeurceramsoc.2021.12.017.